Fluorite-related iridate Pr_3IrO_7: crystal growth, structure, magnetism, thermodynamic, and optical properties

Harish Kumar[1,*], M Köpf[1], A Ullrich[2], M Klinger[3], A Jesche[3] and C A Kuntscher[1,*]

[1] Experimentalphysik II, Institute of Physics, Augsburg University, 86159 Augsburg, Germany
[2] Experimentalphysik IV, Institute of Physics, Augsburg University, 86159 Augsburg, Germany
[3] Experimentalphysik VI, Center of Electronic Correlations and Magnetism, Augsburg University, 86159 Augsburg, Germany

E-mail: harish.kumar@physik.uni-augsburg.de and christine.kuntscher@physik.uni-augsburg.de

Abstract

Spin–orbit coupling in heavy 5*d* metal oxides, in particular, iridates have received tremendous interest in recent years due to the realization of exotic electronic and magnetic phases. Here, we report the synthesis, structural, magnetic, thermodynamic, and optical properties of the ternary iridate Pr_3IrO_7. Single crystals of Pr_3IrO_7 have been grown by the KF flux method. Structural analysis shows that Pr_3IrO_7 crystallizes in an orthorhombic phase with *Cmcm* symmetry. The electron energy loss spectroscopy study indicates that Pr is in a 3+ valence state, which implies a 5+ oxidation state of Ir. Magnetization data measured at high and low magnetic fields do not exhibit any bifurcation between M_{ZFC} and M_{FC}, however, a weak hump in $M(T)$ is observed at $T^*\sim$10.4 K. The specific heat data reveal two maxima at ∼253 and ∼4.8 K. The optical conductivity $\sigma_1(\omega)$ spectrum shows 24 infrared-active phonon modes and reveals an insulating behavior with an optical gap Δ_{OP} of size ∼500 meV. During cooling down, the temperature-dependent reflectivity spectrum reveals eight extra phonon modes below the structural phase transition (∼253 K). An anomaly is observed at around T^* in the temperature evolution of infrared-active mode frequencies suggesting the presence of significant spin–phonon coupling in the system.

Keywords: iridates, magnetic ordering, crystal structure, optical conductivity

1. Introduction

In recent years, iridates have drawn much attention due to a variety of exotic properties arising from the presence of spin–orbit coupling (SOC), on-site Coulomb (U), and crystal field (Δ_{CFE}) interactions of comparable strength [1, 2]. As compared to the 3*d* transition metal oxides, iridates exhibit a large SOC and smaller U due to the heavy and extended nature of the 5*d* orbitals, respectively. In iridates, the comparable energy strength of SOC, U, and Δ_{CFE} creates a fragile balance between interactions that are predicted to host the novel topological phases i.e. Mott insulator, Weyl semimetal and axion insulator [3–6]. Experimentally and theoretically, these interactions have been extensively studied in the context of tetravalent Ir^{4+} ($5d^5$) within the single particle scenario, where the strong SOC splits the Ir t_{2g} states into a completely filled $J_{eff} = 3/2$ band and a half-filled $J_{eff} = 1/2$ band, which lies close to the Fermi energy. This half-filled $J_{eff} = 1/2$ band further splits into a lower (filled) and an upper (empty) Hubbard

* Authors to whom any correspondence should be addressed.

band due to the presence of small U, thus leading to a $J_{eff} = 1/2$ Mott state [7–9]. In contrast, the Ir^{5+} ions have four 5d electrons, the $J_{eff} = 3/2$ band is expected to be fully filled and the $J_{eff} = 1/2$ band to be empty, leading to a nonmagnetic $J_{eff} = 0$ state in the strong SOC limit. However, recent theoretical and experimental studies have shown strong evidence against the SOC driven $J_{eff} = 0$ state [10–15]. The magnetism in the Ir^{5+} $J_{eff} = 0$ picture under strong SOC is thus debatable.

Generally, the 5d Ir based ternary oxide materials with chemical composition A_3IrO_7 (A = rare-earth metal) belong to the family of pentavalent (Ir^{5+}) iridates. These materials basically belong to the class of the defect-fluorite structure with orthorhombic *Cmcm* symmetry in which the Ir^{5+} ions form IrO_6 octahedra and are arranged in one-dimensional chains along the c axis [16–18]. Previously, the structural, magnetic and thermal properties for A_3IrO_7 (A = Pr, Nd, Sm, and Eu) compounds have been studied in the polycrystalline form, in addition, a single crystal study of Pr_3IrO_7 is reported for the electrocatalyst properties [17–19]. The specific heat data for (Pr, Nd, Sm and Eu)$_3IrO_7$ exhibit a thermal anomaly at 261, 342, 420, 485 K, respectively, which has been later assigned to a structural phase transition [17, 18]. It was reported that among these materials only Nd_3IrO_7 reveals an antiferromagnetic (AFM) transition at around 2.6 K [17].

In the present work, we report the synthesis and characterization of Pr_3IrO_7 single crystals. Molten KF flux method has been used to grow the Pr_3IrO_7 single crystals, which were characterization by Laue x-ray diffraction, electron energy loss spectroscopy, magnetization, specific heat, and infrared reflectivity measurements. The obtained magnetization data show a weak hump at $T^* \sim 10.4$ K and a continuous rise below 5.6 K with lowering the temperature. The $M(T)$ data measured at low and high fields do not exhibit any bifurcation between M_{ZFC} and M_{FC} either. Our specific heat results exhibit two maxima at ∼253 and ∼4.8 K. The infrared reflectivity measurements show several infrared-active phonon modes, and the low reflectivity value in the low-frequency range implies an insulating behavior for Pr_3IrO_7. The temperature evolution of the phonon modes clearly reveal a change across the structural phase transition and a hump around T^*.

2. Experimental details

High-quality ingredient powder materials Pr_6O_{11} and IrO_2 with a phase purity of more than 99.99% (M/s Sigma-Aldrich) were mixed in their stoichiometric ratios with a slight excess of IrO_2 and ground well. A pre-heat treatment was performed for the starting material Pr_6O_{11} at 800 °C for ∼8 h to remove any residual atmospheric moisture. The powder mixture was subsequently pelletized and sintered in air at temperatures 950 °C–1130 °C for several days with intermediate grindings. Single crystals of Pr_3IrO_7 were grown by KF flux method using polycrystalline sample (slight excess of IrO_2) and KF flux in a ratio of 1:200. For the crystal growth, the sample was heated at 1100 °C for 4 h and slowly cooled to 850 °C at a rate of 2 °C h^{-1}. Many small crystals were found at the wall of the Pt-crucible (left inset of figure 1(a)). The crystals were removed from the residual KF by rinsing them out with water. The structure and chemical composition of Pr_3IrO_7 samples were analysed using powder x-ray diffraction (XRD) and energy dispersive analysis of x-ray (EDX) using a ZEISS Crossbeam 550/550L scanning electron microscope with an Oxford detector. To check the purity of the crystals, powder XRD was performed on the powder of the crystals using a Rigaku diffractometer (Model: Miniflex 600) with CuK_α radiation in 2θ range 10°–90° with a step of 0.02°. The XRD data were analysed by Rietveld refinement using the FULLPROF program. To further check the purity of the crystals, x-ray Laue diffraction experiments were performed, confirming the high crystallinity of the crystals.

The transmission electron microscopy including electron energy-loss spectroscopy (EELS) was carried out with a JEOL NEOARM F200 instrument, equipped with a Gatan OneView camera and a Continuum S EELS spectrometer. The EELS analysis was done at 200 keV beam energy in the DualEELS™ mode. DC magnetization data were collected from 1.8 to 300 K using a superconducting quantum interference device (SQUID, Quantum Design) magnetometer MPMS. Specific heat data were measured in the temperature range from 1.8 to 300 K using Quantum Design PPMS DynaCool with a heat pulse relaxation method. The temperature-dependent reflectance measurements were carried out in the temperature range 300–5.4 K and frequency range 126–20 000 cm^{-1} using a CryoVac Konti cryostat attached to a Bruker Vertex v80 Fourier transform infrared spectrometer and an infrared microscope (Bruker Hyperion). A thin silver layer was evaporated on half of the crystal, which served as reference to obtain the absolute reflectivity. The frequency resolution was set to 2 cm^{-1} in the far-infrared range, while a resolution of 4 cm^{-1} was chosen for the higher-frequency range. For the analysis, the measured reflectivity spectrum was extrapolated in the low- and high-energy regime by Lorentz fitting and x-ray optic volumetric data, respectively [20]. Note that a power-law ω^n interpolation with an integer $n = 3$ was used to cover the region between measured reflectivity and calculated high-energy extrapolated data. The so-obtained reflectivity spectrum was used to obtain the real part of the optical conductivity $\sigma_1(\omega)$ and the loss function $-\mathrm{Im}(1/\epsilon)$ using the Kramers–Kronig relations and a Lorentz model was used to fit the optical spectra using the RefFIT program [21].

3. Results and discussions

3.1. Structural Analysis

The room-temperature XRD pattern of Pr_3IrO_7 together with the Rietveld refinement is shown in figure 1(a). The refinement analysis confirms that Pr_3IrO_7 is in a single phase and crystallises in an orthorhombic phase with *Cmcm* symmetry (space group 63). The unit cell parameters a, b and c are found to be 10.97 Å, 7.42 Å and 7.53 Å, resp., which match the reported values [17]. We have confirmed the crystallographic planes for Pr_3IrO_7 single crystal through Laue diffraction,

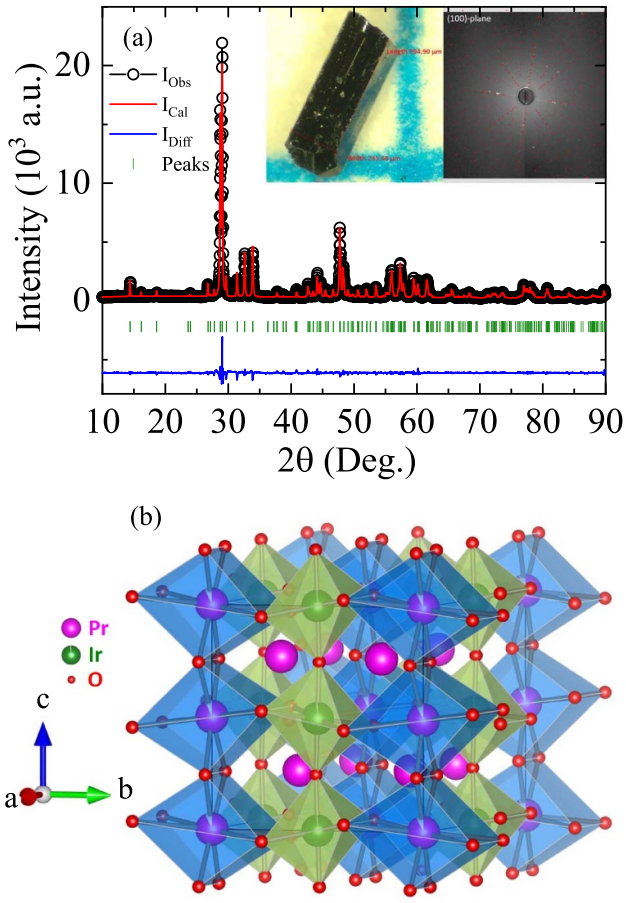

Figure 1. (a) Room-temperature XRD pattern along with Rietveld refinement for Pr_3IrO_7. Right and left inset show crystal image and x-ray Laue diffraction pattern of the Pr_3IrO_7 single crystal, respectively. (b) Crystal structure of Pr_3IrO_7 with the $Pr(1)O_8$ pseudocubes (blue) and IrO_6 octahedra (green).

which insures that Pr_3IrO_7 crystals are in a unique crystalline domain (right inset of figure 1(a)). Figure 1(b) shows the schematic representation of the crystal structure of Pr_3IrO_7, where the Ir cations are six-fold coordinated and form one-dimensional chains of the corner-sharing IrO_6 octahedra along the c axis. The Pr cations are eight-fold coordinated and form a chain of eightfold-distorted $Pr(1)O_8$ cubes, which simultaneously share the edges with the chains of IrO_6 octahedra. The remaining Pr(2) cations lie in between the $Pr(1)O_8$ pseudocubes and IrO_6 octahedra [17].

3.2. Electron energy loss spectroscopy

In this class of oxide materials, understanding the valence state of rare-earth/transition metals is very important, since they play an important role governing the electronic, magnetic, and optical properties. As precursors, Pr_6O_{11} and IrO_2 are used for the sample preparation. In Pr_6O_{11}, Pr exists in a mixed valence state of 3+/4+, i.e. 3+ for Pr_2O_3 and 4+ PrO_2 [22]. In order to understand the Pr cationic charge state in Pr_3IrO_7, electron energy loss spectroscopy (EELS) measurements have been performed on fine powder of Pr_3IrO_7 single crystals. The Pr_2O_3 material with phase purity of >99.9% was used as reference sample for the Pr 3+ charge state. The low loss spectra of the Dual EELS have been used for precise calibration of the zero-point. To process the EELS data, a power-law background fitting has been used. Furthermore, the spectra have been recorded as line scans for five different regions of each sample and analyzed. Figures 2(a) and (b) show the Pr M_4 and M_5 edge absorption spectra for Pr_2O_3 and Pr_3IrO_7, respectively.

The $M_{4,5}$ white lines of Pr correspond to the electronic transitions between the initial state $3d$ and the unoccupied $4f$ orbitals. For Pr_2O_3, the $M_{5,4}$ white lines are observed around 931.3 eV and 950.8 eV, respectively. A shoulder is present on the left side of the Pr M_4 edge, which is indicative for the Pr 3+ valence state [22–25]. As evident in figure 2, the line shape and peak position of the $M_{5,4}$-edge for Pr_3IrO_7 are similar to the $M_{5,4}$-edge spectra of Pr_2O_3. A small chemical shift in the Pr M_5 and M_4 edge is observed, which amounts to ∼0.16 eV and ∼0.23 eV, resp., toward the low energy side, however, the shift is small. A shoulder is also found for Pr_3IrO_7 on the left side of the Pr M_4 edge. For the Pr 4+ valence state, the two peaks have been previously reported on the right side of both

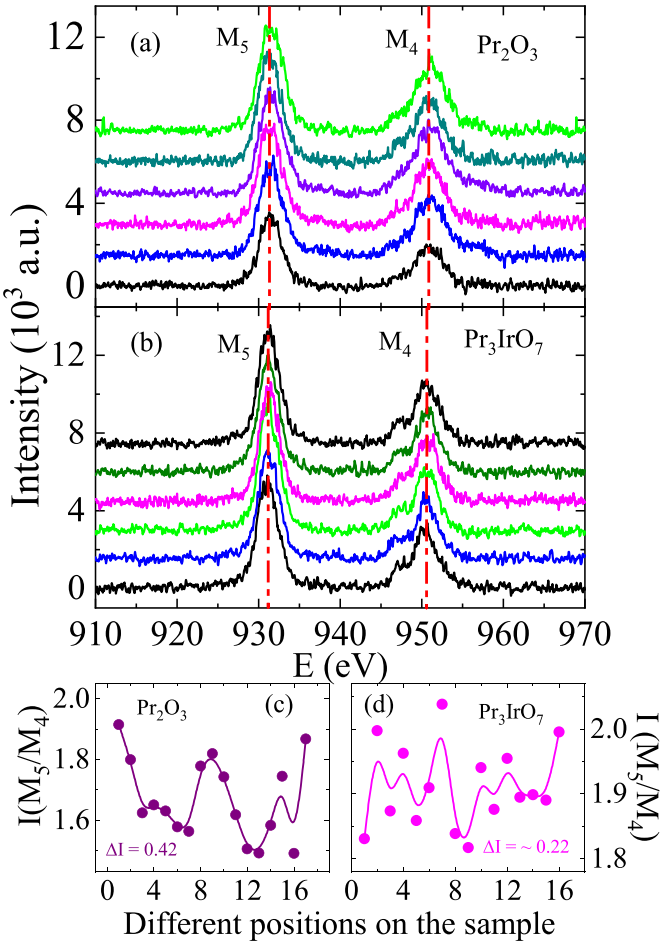

Figure 2. (a) and (b) EELS spectra as a function of energy for the Pr-M_4 and M_5 edges of Pr_2O_3 and Pr_3IrO_7, respectively. (c) and (d) Relative intensity ratios of the Pr M_5 and M_4 edges at different positions of the Pr_2O_3 and Pr_3IrO_7 samples, respectively.

Pr M_5 and M_4 edges around ∼935 eV and ∼955 eV. These are distinctly absent for the present Pr_3IrO_7 sample, which also suggests that Pr is in a 3+ valence state [23, 24]. Furthermore, we have analyzed all the other recorded regions of each sample (not shown). We have found similar types of signatures i.e. a similar amount of chemical shift in Pr $M_{5,4}$ edges, the absence of two peaks on the right side of both Pr M_5 and M_4 edges, and the presence of a shoulder on the left side of Pr M_4 edge. Additionally, we have further looked at the intensity ratio I_{M_5}/I_{M_4} for both Pr_2O_3 and Pr_3IrO_7 materials in figures 2(c) and (d), respectively. The intensity ratio for Pr_2O_3 shows no systematic variation at different position of the sample, and the change in I_{M_5}/I_{M_4} lies between 1.5 to 2 according to figure 2(c). For Pr_3IrO_7, we observe a complete fluctuation in I_{M_5}/I_{M_4} ratio (see figure 2(d)), however, these fluctuations lie in the same range as for Pr_2O_3. Similar types of variation have been found in I_{M_5}/I_{M_4} for other regions of the Pr_3IrO_7 sample (not shown). These results imply that Pr is in 3+ valence state, which points to a 5+ charge state of Ir.

3.3. Magnetization study

Figure 3 shows the temperature-dependent dc magnetization $M(T)$ data for Pr_3IrO_7, measured for the magnetic field orientation $\mathbf{H} \parallel \mathbf{c}$ at 0.5, 1, 2, and 5 kOe magnetic fields by following zero field-cooled (ZFC) and field-cooled (FC) protocols. As evident in the figure 3, the magnetic moment in the field of 0.5 kOe increases with decreasing temperature and exhibits a broad (weak) hump in the particular temperature range of ∼22 to ∼5.6 K and centered around $T^* \sim$ 10.4 K. Upon further cooling the magnetization increases continuously from 5.6 K to the lowest measured temperature. For a spin-glass behavior, the magnetization is expected to exhibit a bifurcation between M_{ZFC} and M_{FC} and an anomaly in M_{ZFC} across the glassy temperature, which shifts to lower temperature with increasing the field [11]. Our $M(T)$ does not show any such bifurcation between M_{ZFC} and M_{FC} in the whole temperature range, which rules out the possibility of a glassy phase. The left inset of figure 3 depicts the low-temperature ZFC magnetization data for H = 0.5 kOe, which clearly shows the presence of a hump around ∼10.4 K and a prominent change around ∼5.6 K, as highlighted by the arrow. The $M(T)$ data measured at higher magnetic fields (1, 2, and 5 kOe) reveal that the weak hump becomes more prominent with increasing magnetic field (figure 3). As evident in the high field $M(T)$ data, with increasing the field the moment below ∼5.6 K increases continuously and exhibits a clear change in curvature of $M(T)$ in that particular temperature regime.

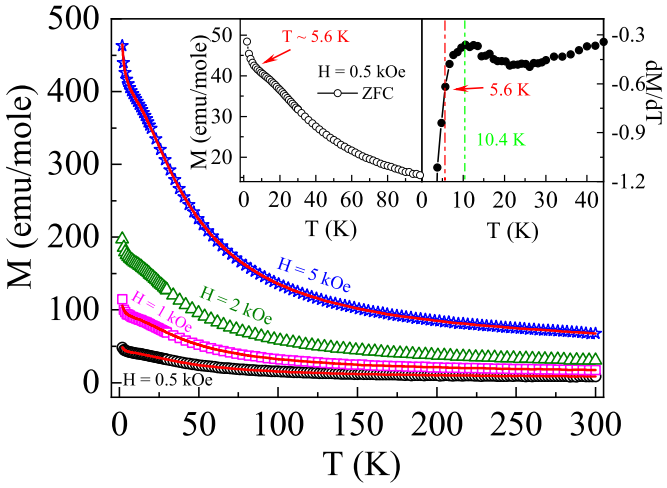

Figure 3. Temperature dependence of the dc magnetization following a ZFC and FC protocol at magnetic fields of 0.5, 1, 2 and 5 kOe for Pr_3IrO_7. The open symbols and line represent the ZFC and FC magnetic curves, respectively. Left inset: $M_{ZFC}(T)$ data measured at 0.5 kOe, where the red arrow marks the temperature 5.6 K. Right inset: temperature derivative dM/dT at a magnetic field of 0.5 kOe.

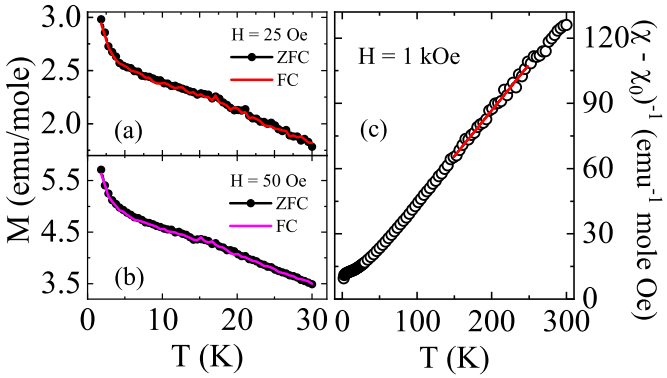

Figure 4. DC magnetization data as a function of temperature for Pr_3IrO_7 measured in low magnetic fields (a) 25 Oe and (b) 50 Oe using the ZFC and FC protocol. (c) Temperature-dependent inverse susceptibility $(\chi - \chi_0)^{-1}$ deduced from the M_{ZFC} data for Pr_3IrO_7, where the solid red line represents a linear fitting describing a modified Curie–Weiss behavior as defined in the text.

For a more detailed analysis, we have plotted the first derivative of the $M_{ZFC}(T)$ magnetization (dM/dT) in the right inset of figure 3 for 0.5 kOe field data. The dM/dT data distinctly show a sharp drop below ∼5.6 K, and a clear change in the curvature of $M(T)$ at T^* in the temperature range of 22 K to 5.6 K. This weak hump in $M(T)$ could be associated with the magnetic degree of freedom, which leads to a significant deviation in magnetic susceptibility from the Curie–Weiss behavior at low temperature (see figure 4(c)). It is interesting to note that a similar type of weak hump in magnetization data has been seen for other Pr based perovskites $PrBO_3$ (B = transition metals) at low temperature where the rare-earth spins order in an AFM arrangement [26–29]. The continuous increase in magnetization below T^* could be associated with a minor paramagnetic (PM) impurity phase consisting of non-interacting and isolated Pr or Ir moments. To obtain further insight into the low-temperature magnetic state of Pr_3IrO_7, we have measured $M(T)$ at low fields 25 and 50 Oe (see figures 4(a) and (b), respectively). The $M(T)$ data at the low field also exhibit a continuous increase in moment across the same temperature (∼5.6 K), as observed in high field measurements, however, the weak hump around ∼10.4 K is not clearly visible. The notable observations in the $M(T)$ data occur at low field, namely, (a) no change in the temperature, where the magnetization continuously increases, (b) increase in magnetic moment with increasing fields, and (c) no hysteresis between M_{ZFC} and M_{FC}.

Figure 4(c) depicts the temperature-dependent inverse magnetic susceptibility ($\chi^{-1} = (\mathrm{H\,M^{-1}})$), which is deduced from the M_{ZFC} data (figure 3). The $\chi^{-1}(T)$ data have been analyzed using a modified Curie–Weiss (CW) law in the temperature range 150–248 K [30], according to:

$$\chi(T) = \chi_0 + \frac{C}{(T - \theta_{CW})}, \tag{1}$$

where χ_0, C, and θ_{CW} are the temperature-independent magnetic susceptibility, the Curie constant, and Curie–Weiss temperature, respectively. The $(\chi - \chi_0)^{-1}$ vs T plot shows a linear behavior in the high temperature regime (see figure 4(c)).

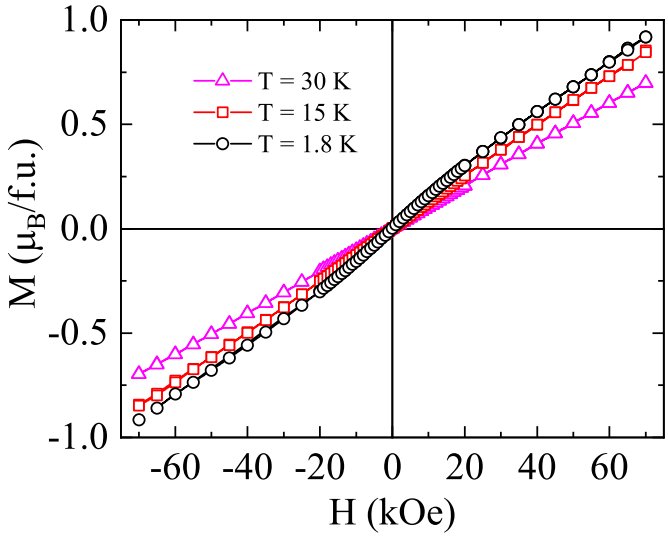

Figure 5. Magnetic field-dependent magnetization $M(H)$ collected at 1.8, 15, and 30 K.

The fitting of $\chi(T)$ with equation (1) gives $\chi_0 = 9.5\times10^{-3}$ emu mole^{-1}, $C = 2.36$ emu K mole^{-1}, and $\theta_{CW} = -5.7$ K. The magnitude of θ_{CW} is close to T^*. The negative sign of θ_{CW} and its magnitude suggest AFM type interactions in Pr_3IrO_7. From the obtained Curie constant C, the effective paramagnetic moment (μ_{eff}) is calculated and found to be 4.34 μ_B/f.u., and hence 2.5 μ_B/Pr, which is low compared to the theoretically expected moment ($\mu_{eff} = g\sqrt{J(J+1)}$) value 3.58 μ_B, where the Lande g factor and the J value for Pr^{3+} ($4f^2$) electronic configuration are 4/5 and 4, respectively. The observed low moment (μ_{eff}) implies that the four d-electrons of Ir^{5+} ($5d^4$ electronic state) occupy completely $J_{eff} = 3/2$ quartet state, which means $\mu_{eff} = 0$ for the Ir^{5+} state. This low moment (μ_{eff}) discrepancy with expected moment has been seen in other Pr-based ternary oxide Pr_3MO_7 (M = Nb, Ta and Sb) materials [16].

The magnetic field-induced magnetic behavior in Pr_3IrO_7 below and above T^* was characterized in terms of the isothermal magnetization as a function of magnetic field (H) for $\mathbf{H} \parallel c$ at various temperatures in the field range of ±70 kOe, and the results are shown in figure 5. It is evident that the $M(H)$ data do not show any sign of saturation for all temperatures up to the maximum applied field, i.e. 70 kOe. Accordingly, the $M(H)$ data above T^* exhibit a linear behavior like PM. In contrast, the $M(H)$ curve at 1.8 K exhibits a linear behaviour up to about ∼20 kOe, and above this field the $M(H)$ data show a slight deviation from the linearity with field. Furthermore, the absence of any hysteresis in the $M(H)$ curve at 1.8 K suggests that the magnetic ground state is neither a ferromagnetic nor spin-glass but could be AFM type. The magnetic moment at 1.8 K and 70 kOe is found to be 0.92 μ_B/f.u.; this value is low compared to the expected moment ($\mu_H = gJ\mu_B$), which is calculated as 3.2 μ_B, where g and J are 4/5 and 4 for Pr^{3+} ($4f^2$) electronic configuration. This low values of the magnetization and the μ_{eff} in Pr_3IrO_7 may be due to the crystal field splitting of the Pr^{3+} ion because of the site symmetry of Pr(1) and Pr(2) ions [16, 31], which needs to be understood through microscopic probe.

3.4. Specific heat capacity

For a better understanding of the thermodynamic behavior in the vicinity of the observed weak hump in the $M(T)$ data, the specific heat capacity C as a function of temperature has been measured down to 1.8 K. Figure 6 shows the obtained specific heat capacity $C(T)$ in the form of a C/T *vs* T plot. The $C(T)$ data exhibit two maxima/peaks: one in the high temperature (∼253 K) and one in the low temperature (∼4.8 K) regime. The latter could be related to the weak hump of $M(T)$ (that manifest the maxima at ∼10.4 K), however, the small shift in temperature is not clear at the moment. A similar low-temperature change in $C(T)$ data is also present in a previous study but it has not been discussed so far [17]. The observed high-temperature maxima around ∼253 K is close to the reported value of the Pr_3IrO_7 polycrystalline sample, where it was related to a structural phase transition from orthorhombic to monoclinic [17, 18].

Furthermore, the magnetic contribution (C_m) to the total heat capacity is calculated by subtracting its lattice (phonon) contribution (C_l) from C. The C_l is determined by fitting of the $C(T)$ data from 30 to 150 K using a combined Debye–Einstein model ($C_l = C_{\text{Debye}} + C_{\text{Einstein}}$). The C_{Debye} and C_{Einstein} terms are given as [11, 32]:

$$C_{\text{Debye}} = a_1\left[9R\left(\frac{T}{\theta_D}\right)^3\int_0^{\theta_D/T}\frac{x^4e^x}{(e^x-1)^2}dx\right], \quad (2)$$

$$C_{\text{Einstein}} = 3R\sum_{i=1}^{3}b_i\left[\left(\frac{\theta_{Ei}}{T}\right)^2\frac{e^{\theta_{Ei}/T}}{\left(e^{\theta_{Ei}/T}-1\right)^2}\right], \quad (3)$$

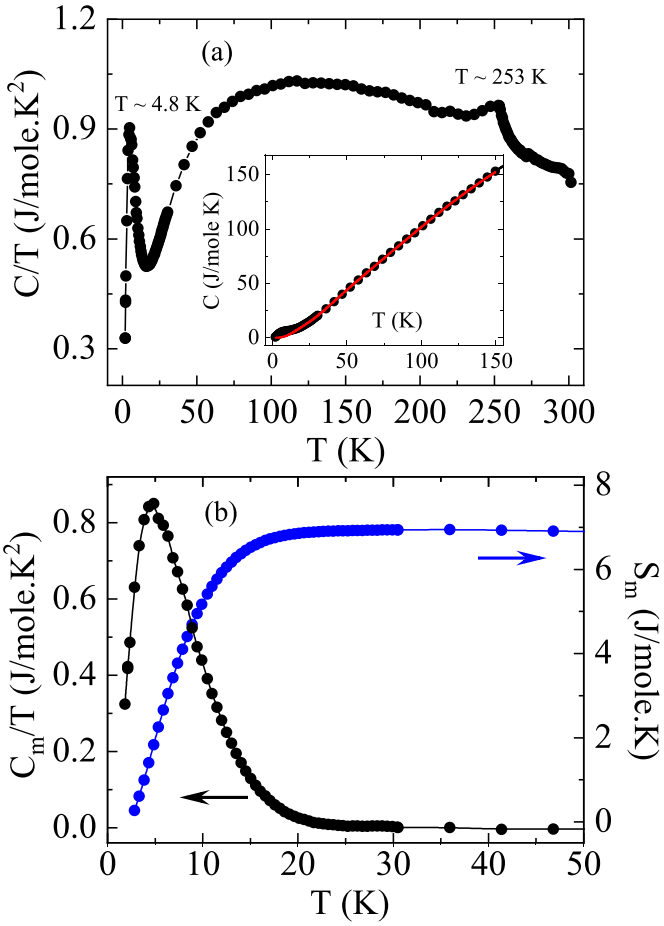

Figure 6. (a) Temperature-dependent specific heat (C/T) of Pr_3IrO_7. The inset shows $C(T)$ along with the lattice contributions (solid red line) obtained from fitting with the combined Debye and Einstein model. (b) Temperature-dependent magnetic specific heat (C_m/T) (left panel) and the calculated magnetic entropy with temperature $S_m(T)$ (right panel).

where R is the universal gas constant, and θ_D and θ_E are the Debye and Einstein temperature, respectively. The a_1 and b_i coefficients are the weighting factors corresponding to acoustic and optical phonons (Debye and Einstein coefficients), respectively. The $C(T)$ data can be fitted well with one Debye and three Einstein (1D + 3E) terms of lattice specific heat and is represented by a solid line in the inset of figure 6(a). The obtained C_l is extrapolated down to 1.8 K for C_m. From the combined fitting, the Debye and Einstein temperatures θ_D, θ_{E_1}, θ_{E_2} and θ_{E_3} are found to be 94.6 K, 493.7 K, 201.6 K, and 728 K, resp., and the associated weighing factors a_1, b_1, b_2, and b_3 are fixed in the ratio of 1, 5, 3, and 2, respectively. The total sum of coefficients $a_1 + \sum b_i$ matches well with the total number of atoms in the formula unit in Pr_3IrO_7. The obtained magnetic specific heat (C_m) is shown in the left panel of figure 6(b) in the form of a $C_m T^{-1}$ *vs* T plot. The magnetic specific heat shows a clear broad peak around ~4.8 K, which is close to T^* where the weak magnetic hump is observed in the $M(T)$ data.

To understand this further through the change in entropy, the magnetic entropy S_m is calculated by integrating C_m/T with T according to:

$$S_m(T) = \int_0^T \frac{C_m(T)}{T} dT. \quad (4)$$

The change in magnetic entropy with temperature $S_m(T)$ is shown in the right panel of figure 6(b). Accordingly, S_m almost saturates at ~6.9 J mole^{-1} K above ~22.2 K, which is close to the the temperature (~22 K) below which the magnetization shows a change in its curvature. We have calculated the expected entropy change due to the Pr^{3+} ions with $J = 4$ and found it to be 18.2 J (mole K)$^{-1}$ [$R \ln(2J + 1)$]. The obtained S_m is low and about 37.9% of the theoretical value. This lower value of S_m may be due to the higher alignment of crystal field effect levels around 22 K.

3.5. Optical conductivity

For the characterization of the electronic and vibrational properties of Pr_3IrO_7, we carried out reflectivity measurements in the infrared frequency range. The temperature-dependent reflectivity spectrum over the whole measured frequency range is shown in figure 7(a) at various temperatures, while the corresponding optical conductivity σ_1 is displayed in

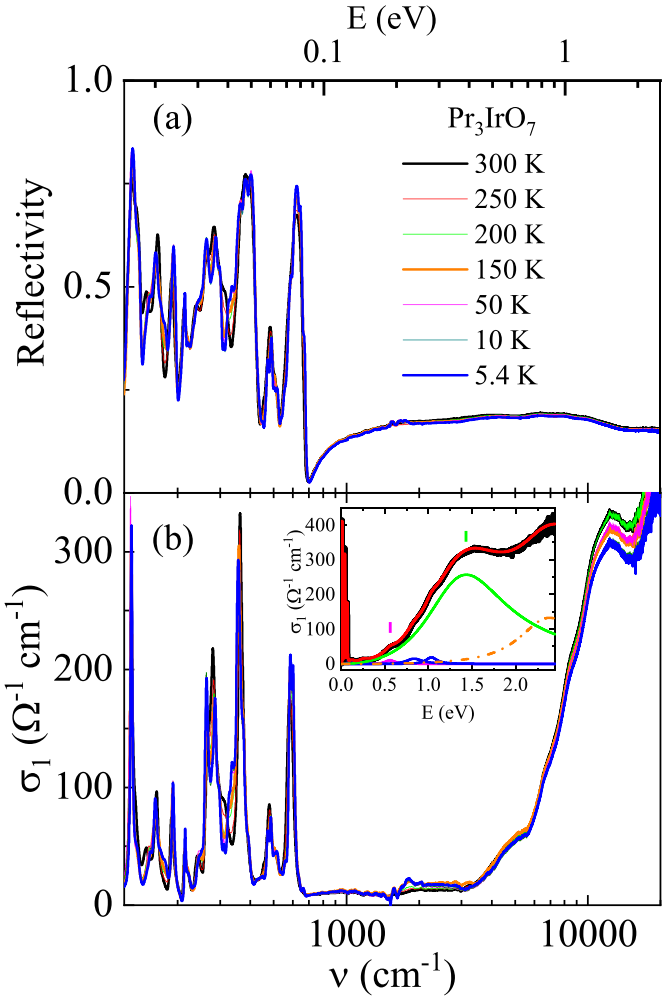

Figure 7. (a) Reflectivity and (b) optical conductivity (σ_1) of Pr_3IrO_7 at various temperatures in the whole measured frequency range. Inset in (b): room-temperature optical conductivity σ_1 together with the Lorentz fit and the individual Lorentz contributions.

figure 7(b). Pr_3IrO_7 crystallises in an orthorhombic phase with *Cmcm* symmetry. According to the factor group analysis for the *Cmcm* structure symmetry, the irreducible representation of optical active phonons is given as:

$$\Gamma_{optic} = [10B_{1u} + 12B_{2u} + 10B_{3u}]_{IR} + [8A_g + 8B_{1g} + 5B_{2g} + 6B_{3g}]_R, \quad (5)$$

where *IR* (*R*) indicates the infrared-active (Raman-active) modes. Theoretically, 32 infrared-active phonons are expected for Pr_3IrO_7 due its *Cmcm* structure symmetry, see table 1. Note that all Pr, Ir and O atoms in Pr_3IrO_7 are involved in these lattice vibrations. From the room temperature low-energy optical conductivity spectrum σ_1, two main observations can be made: First, the overall low value of σ_1 in the far-IR region, which signals the insulating character of Pr_3IrO_7. Second, 24 IR-active transverse phonon modes can be resolved and noted in table 2. In analogy to the related compound Gd_3NbO_7 [33] the modes above ∼190 cm^{-1} can be ascribed to stretching and

Table 1. Wyckoff positions and Γ point representations for *Cmcm* (No. 63) space group.

Atoms	Wyckoff positon	Γ representation
Pr(1)	4 *a*	$2B_{1u} + 2B_{2u} + B_{3u}$
Pr(2)	8 *g*	$B_{1u} + 2B_{2u} + 2B_{3u}$
Ir	4 *b*	$2B_{1u} + 2B_{2u} + B_{3u}$
O(1)	16 *h*	$3B_{1u} + 3B_{2u} + 3B_{3u}$
O(2)	8 *g*	$B_{1u} + 2B_{2u} + 2B_{3u}$
O(3)	4 *c*	$B_{1u} + B_{2u} + B_{3u}$

bending vibrations of IrO_6 octahedra, and the modes below ∼190 cm^{-1} can be assigned to translational modes of the Pr^{3+} and Ir^{5+} ions.

The onset of electronic excitations in the optical conductivity spectrum (see inset of figure 7(b)) is located at around 0.5 eV, which can serve as an estimate of the optical gap, Δ_{OP} ∼500 meV. The size of Δ_{OP} is comparable to that in the honeycomb-type iridates Na_2IrO_3 and α-Li_2IrO_3 with Ir $5d^5$ electronic configuration [34, 35]. The high-energy σ_1 spectrum shows weak Lorentz contributions located at ∼0.56 eV, ∼0.83 eV, and ∼1.03 eV and a stronger contribution ∼1.43 eV. In analogy to other iridates [35–39], these excitations can be ascribed to on-site and inter-site transitions between $J_{eff} = 1/2$ and $J_{eff} = 3/2$ states, which could show additional splittings due to octahedral distortion. The Lorentz term at ∼2.4 eV can be attributed to charge-transfer excitations between the Ir 5*d* and O 2*p* orbitals.

It is furthermore intriguing to compare the high-energy σ_1 spectrum of Pr_3IrO_7 with that of insulating Li_2RuO_3, where Ru^{4+} has a $4d^4$ electron configuration similar to Ir^{5+} ($5d^4$), however, with a smaller SOC and higher *U*-value [40]. Interestingly, for Li_2RuO_3 one observes a similar gap size Δ_{OP} ∼600 meV, and the excitations around ∼0.95 and ∼1.46 eV are slightly blueshifted in energy [40], which might be due to the different SOC strength. In addition, it has been seen in a local probe study that the Ir^{5+} systems exhibit higher angular strength of the SOC, $< \mathbf{L} \cdot \mathbf{S} >$, compared to the Ir^{4+} state [41]. Therefore, in the context of SOC, more investigations employing theoretical calculations are required to understand the electronic excitations in the strong SOC limit in Ir^{5+}-based oxides.

Furthermore, we checked the possible impact of the structural phase transition at ∼253 K and the magnetic ordering at T^* on the vibrational and electronic excitations. The temperature-dependent reflectivity spectrum of Pr_3IrO_7 is shown in figure 8(a) at various temperatures in the far-infrared range, since here the pronounced changes occur. With decreasing temperature, we observe several changes, namely the appearance of eight additional transverse IR modes at 167.5 (20.7), 177.9 (22.0), 229.8 (28.5), 306.7 (38.0), 337.1 (41.7), 471.1 (58.4), 517.3 (64.1), 628.3 (77.8) cm^{-1} (meV) around 250 K in the far-infrared range (table 2), a large change in the observed modes in the frequency range 290–350 cm^{-1} (especially for the 314.1 cm^{-1} mode), and the IR modes become sharper at low temperature. These changes are also clearly

Table 2. Observed transverse and longitudinal IR phonon mode frequencies (in cm^{-1}) for Pr_3IrO_7 at 30, 20, and 5.4 K.

Transverse phonon frequencies			Longitudinal phonon frequencies		
300 K	200 K	5.4 K	300 K	200 K	5.4 K
128.4	128.4	128.7	132.8	134.1	134.4
133.0	135.8	135.3	140.6	140.6	141.1
148.1	151.6	153.2	151.2	153.0	154.2
163.6	161.4	161.4	173.1	170.2	166.9
188.8	167.5	169.6	195.8	174.8	175.4
193.6	177.9	177.2	204.2	178.9	179.7
212.9	189.9	191.5	215.3	197.2	198.5
218.6	202.5	201.7	219.5	203.4	204.2
240.3	213.6	214.3	242.9	215.5	216.5
265.5	218.4	221.4	269.4	221.4	222.5
279.9	229.8	232.0	291.4	231.2	233.3
295.5	240.2	243.4	302.4	244.3	245.0
314.1	263.6	263.6	325.1	271.0	270.5
362.7	283.1	284.8	429.3	293.1	293.4
366.1	297.2	297.1	451.4	305.1	304.6
391.5	306.7	311.0	468.0	325.6	327.5
454.2	323.2	324.7	495.5	339.7	340.0
478.9	337.1	335.6	519.2	391.9	391.0
506.7	358.4	357.3	541.0	431.5	426.0
545.0	373.6	373.4	591.0	455.8	451.1
564.2	394.7	394.1	633.0	472.0	477.1
579.8	455.1	454.1	657.0	495.2	495.2
595.8	471.1	471.7	670.7	508.0	506.9
664.6	483.8	485.6	713.7	520.7	524.0
	504.4	504.8		540.6	537.2
	517.3	517.1		557.0	556.6
	542.0	536.6		590.5	593.5
	569.9	554.6		634.4	637.1
	585.3	586.6		660.6	660.3
	601.2	605.0		675.8	679.6
	628.3	636.2		689.8	696.8
	664.7	667.4		715.9	717.2

seen in temperature-dependent conductivity σ_1 spectrum of the far-infrared regime as shown in figure 8(c). The observed additional modes around 250 K are probably due to the structural phase transition which was previously reported [17, 18] and also seen in the above-described heat capacity data (see figure 6(a)). Figure 8(b) shows temperature-dependent loss function in the far-infrared range. The eigenfrequencies of the longitudinal optical phonon modes appear as maxima in the loss function [42]. We found 24 longitudinal phonon modes at room temperature and eight extra modes below the structural phase transition temperature ∼253 K, see table 2, which further confirms the observed extra phonon modes as seen in the optical conductivity spectrum. Like the reflectivity and conductivity spectrum, the temperature-dependent loss function exhibits a large change in the longitudinal modes in the frequency range 285–350 cm^{-1}. Moreover, an additional phonon mode around ∼371.0 cm^{-1} is seen in the loss function spectrum compared to conductivity spectrum. The temperature-dependent σ_1 spectrum in the higher energy region is shown in the figure 7(b). Obviously, the observed Lorentz contributions (∼0.56, ∼0.83, ∼1.03 and ∼1.43 eV) do not show any noticeable change with lowering the temperature. Figure 8(d) shows the frequency position of three selected phonon modes as a function of temperature. The frequency of the modes at 579.8 and 391.5 cm^{-1} show an abrupt increase around 250 K, which we attribute to the structural phase transition occurring at this temperature. All three selected modes show an anomaly at around T^*, where a weak hump is observed in the magnetization data. It is well known that the Dzyaloshinskii-Moriya interaction (DMI) mainly occurs due to the distortions of IrO_6 octahedra which are induced by the presence of strong SOC in iridates [43]. In recent studies, it has been shown that spin-phonon coupling occurs due to the bending of Ir–O–Ir bonds which is mainly mediated by the DMI [44, 45]. For Ln_3IrO_7 (Ln = Pr, Nd, Sm and Eu), it has been reported that both tilt of the IrO_6 octahedra and distortion in the Ir-Ln-O slab increase at the low temperature [18]. Therefore, the observed an anomaly for the IR phonon modes around T^* underlines the importance of spin-phonon coupling in Pr_3IrO_7.

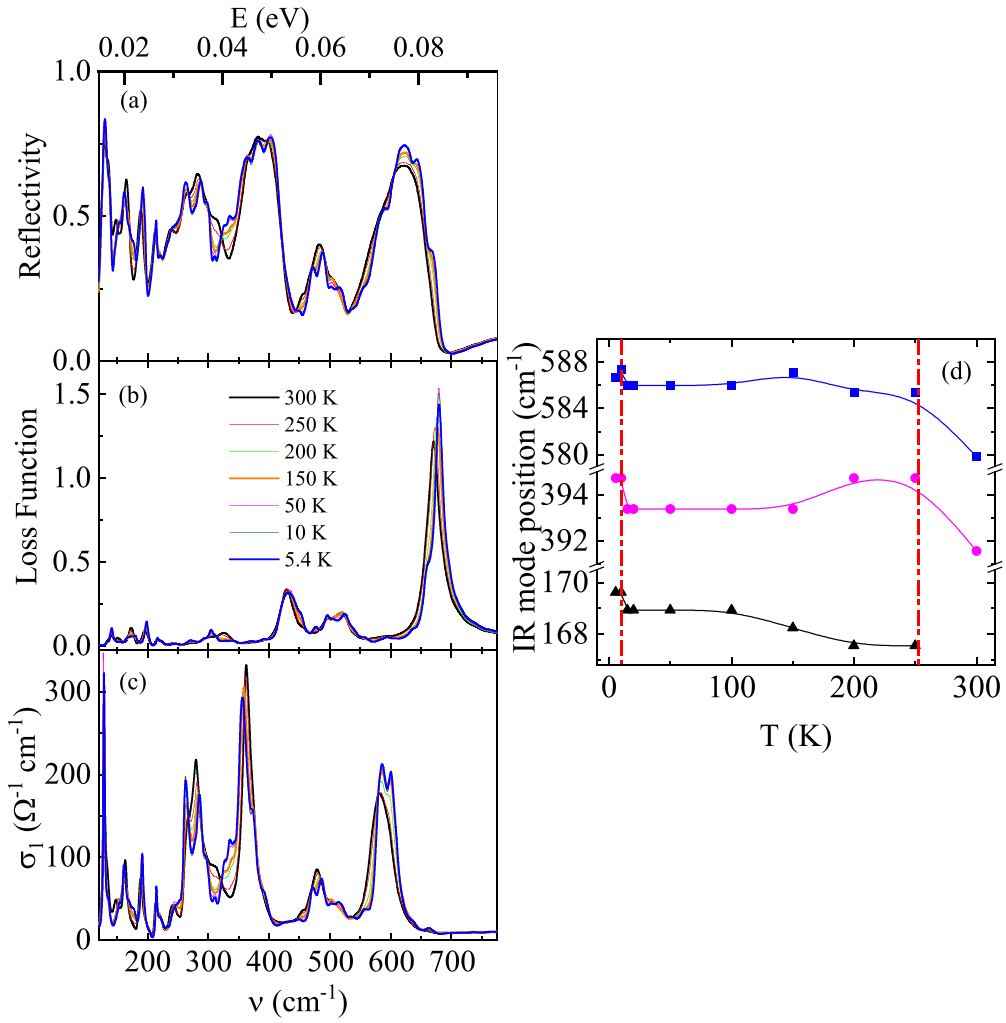

Figure 8. (a) Reflectivity, (b) loss function, and (c) optical conductivity σ_1 at various temperatures in the low-energy range. (d) Temperature evolution of the frequency of three selected phonon modes. The two vertical dashed red lines in (d) mark the T^* and structural phase transition temperature ($\sim$253 K).

4. Conclusion

In summary, the structural, magnetic, thermodynamic, and optical properties are studied in detail for single-crystalline Pr_3IrO_7 ternary iridate. The structural analysis shows that Pr_3IrO_7 crystallizes in the orthorhombic phase with *Cmcm* symmetry. The electron energy loss spectroscopy measurements reveal a 3+ oxidation state for Pr, hence 5+ oxidation state of Ir in Pr_3IrO_7. As a consequence, it represents the ideal system to study the magnetic and electronic evolution of Pr rare-earth. Our magnetic and specific heat results suggest a possible weak low-temperature AFM state for Pr_3IrO_7. Based on the reflectivity data analysis, we conclude an insulating electronic structure for Pr_3IrO_7 with an optical gap $\Delta_{OP} \sim 500$ meV. The temperature-dependent reflectivity spectrum shows eight extra modes below 250 K, which can be attributed to a structural phase transition. Furthermore, several phonon modes reveal an anomaly in the temperature dependence of their frequency position at $T^* \sim 10.4$ K, where a weak hump is observed in the magnetization data, indicative for sizeable spin-phonon coupling in the system.

Data availability statement

The data that support the findings of this study are available upon reasonable request from the authors.

Acknowledgments

H K acknowledges Dr J Ebad-Allah and Dr S Ghara for fruitful discussions. H K acknowledges funding (PDOK-95-19) from the Bavarian Science Foundation and by the Deutsche Forschungsgemeinschaft, Germany, through Grant No. KU 4080/2-1.

ORCID iD

C A Kuntscher https://orcid.org/0000-0002-5454-4535

References

[1] Witczak-Krempa W, Chen G, Kim Y B and Balents L 2014 *Annu. Rev. Condens. Matter Phys.* **5** 57
[2] Rau J G, Lee E K H and Kee H Y 2015 *Annu. Rev. Condens. Matter Phys.* **7** 195
[3] Pesin D and Balents L 2010 *Nat. Phys.* **6** 376
[4] Wan X, Turner A M, Vishwanath A and Savrasov S Y 2011 *Phys. Rev.* B **83** 205101
[5] Ueda K, Kaneko R, Ishizuka H, Fujioka J, Nagaosa N and Tokura Y 2018 *Nat. Commun.* **9** 3032
[6] Ueda K, Fukuda H, Kaneko R, Fujioka J and Tokura Y 2020 *Phys. Rev.* B **102** 245131
[7] Kim B J *et al* 2008 *Phys. Rev. Lett.* **101** 076402
[8] Kim B J, Ohsumi H, Komesu T, Sakai S, Morita T, Takagi H and Arima T 2009 *Science* **323** 1329
[9] Moon S J *et al* 2008 *Phys. Rev. Lett.* **101** 226402
[10] Kharkwal K C, Roy R, Kumar H, Bera A K, Yusuf S M, Shukla A K, Kumar K, Kanungo S and Pramanik A K 2020 *Phys. Rev.* B **102** 174401
[11] Gondh S, Patidar M M, Kumar K, Saravanan M P, Ganesan V and Pramanik A K 2021 *Phys. Rev.* B **104** 014401
[12] Garg C, Roy D, Lonsky M, Manuel P, Cervellino A, Müller J, Kabir M and Nair S 2021 *Phys. Rev.* B **103** 014437
[13] Dey T *et al* 2017 *Phys. Rev.* B **96** 174411
[14] Nag A *et al* 2016 *Phys. Rev. Lett.* **116** 097205
[15] Cao G, Qi T F, Li L, Terzic J, Yuan S J, DeLong L E, Murthy G and Kaul R K 2014 *Phys. Rev. Lett.* **112** 056402
[16] Vente J F, Helmholdt R B and Ijdo D J W 2004 *J. Solid State Chem.* **108** 18
[17] Nishimine H, Wakeshima M and Hinatsu Y 2004 *J. Solid State Chem.* **177** 739
[18] Nishimine H, Doi Y, Hinatsu Y and Sato M 2007 *J. Ceram. Soc. Japan* **115** 577
[19] Wang Y, Liu S, Qin Q, Liu H, Zhang L, Wei T, Li H and Liu X 2021 *Sci. China Mater.* **64** 2193
[20] Tanner D B 2015 *Phys. Rev.* B **91** 035123
[21] Kuzmenko A B 2005 *Rev. Sci. Instrum.* **76** 083108
[22] Kumar H, Kharkwal K C, Kumar K, Asokan K, Banerjee A and Pramanik A K 2020 *Phys. Rev.* B **101** 064405
[23] Richter J, Brauna A, Harveyb A S, Holtappelsa P, Graulea T and Gauckler L J 2008 *Physica B* **403** 87
[24] López-Cartes C, Bernal S, Calvino J J, Cauqui M A, Blanco G, Pérez-Omil J A, Pintado J M, Helveg S and Hansen P L 2003 *Chem. Commun.* **5** 644
[25] Abel J 2012 Corrélations compositions chimiques- structures d'oxydes mixtes (Ce/Zr) á base de Pr4+/Pr3+ et propriétés de réductibilité *PhD Thesis* Institut de Chimie de la Matière Condensée de Bordeaux, France
[26] Kumar A, Warshi M K, Sagdeo A, Krzystyniak M, Rudic S, Adroja D T, Silva I da and Sagdeo P R 2021 *Phys. Rev.* B **104** 035101
[27] Venugopal R B, Vittal P B, Narsinga R G, Chou F C and Suresh B D 2015 *Adv. Mater. Res.* **1086** 96
[28] Mendivil L F, Alvarado-Rivera J, Verdín E, Díaz J A, Mata J, Conde A and Durán A 2020 *Appl. Phys.* A **126** 574
[29] Mendivil L F, Alvarado-Rivera J, Tavizon G, Verdín E, Arenas-Alatorre J and Durán A 2020 *J. Mater. Sci. Mater. Electron.* **32** 24484
[30] Kumar H, Dhaka R S and Pramanik A K 2017 *Phys. Rev.* B **95** 054415
[31] Zhou Z X, Cao G, McCall S, Crow J E, Guertin R P, Mielke C H and Rickel D G 2002 *Phil. Mag.* B **82** 1401
[32] Ghara S, Ter-Oganessian N V and Sundaresan A 2017 *Phys. Rev.* B **95** 094404
[33] Ptak M, Pilarek B, Watras A, Godlewska P, Szczygiel I and Hanuza J 2019 *J. Alloys Compd.* **810** 151892
[34] Comin R *et al* 2012 *Phys. Rev. Lett.* **109** 266406
[35] Hermann V, Ebad-Allah J, Freund F, Pietsch I M, Jesche A, Tsirlin A A, Deisenhofer J, Hanfland M, Gegenwart P and Kuntscher C A 2017 *Phys. Rev.* B **96** 195137
[36] Hermann V, Ebad-Allah J, Freund F, Jesche A, Tsirlin A A, Gegenwart P and Kuntscher C A 2019 *Phys. Rev.* B **99** 235116
[37] Li Y, Foyevtsova K, Jeschke H O and Valenti R 2015 *Phys. Rev.* B **91** 161101
[38] Kim B H, Shirakawa T and Yunoki S 2016 *Phys. Rev. Lett.* **117** 187201
[39] Li Y, Winter S M, Jeschke H O and Valenti R 2017 *Phys. Rev.* B **95** 045129
[40] Yun S 2020 Studies on Transition metal dimers in Li_2RuO_3 *PhD Thesis* Seoul National University, South Korea
[41] Laguna-Marco M A, Kayser P, Alonso J A, Martínez-Lope M J, Veenendaal M van, Choi Y and Haskel D 2015 *Phys. Rev.* B **91** 214433
[42] Klingshirn C F 2012 *Semiconductor Optics* (Berlin: Springer)
[43] Bhatti I N, Rawat R, Banerjee A and Pramanik A K 2014 *J. Phys.: Condens. Matter* **27** 016005
[44] Son J, Park B C, Kim C H, Cho H, Kim S Y, Sandilands L J, Sohn C, Park J G, Moon S J and Noh T W 2019 *npj Quantum Mater.* **4** 17
[45] Kumar H, Sathe V G and Pramanik A K 2019 *J. Magn. Magn. Mater.* **478** 148